ACS APPLIED MATERIALS & INTERFACES

www.acsami.org
Research Article

Heterogeneous Condensation on Simplified Viral Envelope Protein Structures

Kawkab Ahasan, Han Hu, Pranav Shrotriya, and Todd A. Kingston*

Cite This: ACS Appl. Mater. Interfaces 2025, 17, 27829−27838
Read Online

ACCESS | Metrics & More | Article Recommendations | Supporting Information

ABSTRACT: Elucidating the mechanisms of heterogeneous condensation on viral and bacterial envelopes is crucial for understanding biothreat transport phenomena and optimizing capture efficiency in condensation-based detection devices. We investigate the impact of viral envelope geometric parameters [e.g., surface structure pitch-to-diameter ratio (p/d)] due to protruding glycoproteins and surface wettability [via liquid−solid interaction intensity (f)] on heterogeneous condensation using molecular dynamics simulations. Complex glycoprotein structures were modeled as cylindrical pillars to analyze condensation rates and active surface areas across a range of p/d ratios (1.0, 1.2, 1.3, 1.7, 2.0, and ∞) and contact angles (θ = 15°, 75°, and 105°, corresponding to f = 3.0, 2.0, and 1.5) to address envelope geometries for a wide variety of viruses. The results indicate that initial condensation rates on surfaces with intermediate p/d ratios (e.g., 1.2−1.3) are significantly higher due to increased active surface area and droplet cluster formations. The rapid initial condensation fills up the gap between the pillars, reducing the active surface area and leading to a gradual decrease and a plateau in the condensation rate. The increased peak condensation rates are not observed as p/d increased to and above 1.7, as the exhibited behavior is like condensation on the unstructured surface. An increase in surface hydrophilicity (θ = 15°, f = 3.0) leads to faster nucleation and higher peak condensation rates compared to hydrophobic surfaces (θ = 105°, f = 1.5). The influence of viral envelope geometries and surface wettability on the heterogeneous condensation mechanisms offers foundational insights required to understand airborne biothreat transmission, which is particularly important in the atmosphere and respiratory tract, and improve biothreat detection methods utilizing condensation-based capture devices.

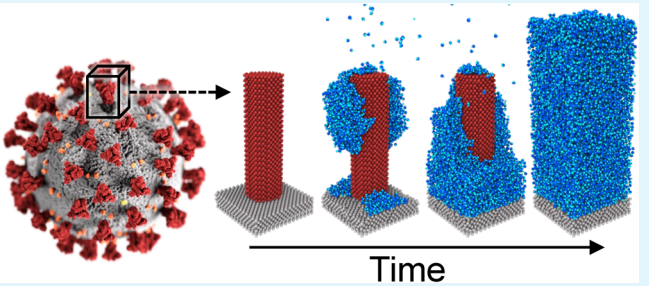

KEYWORDS: *glycoprotein, heterogeneous condensation, heterogeneous nucleation, envelope protein, virus, molecular dynamics*

INTRODUCTION

Heterogeneous condensation occurs in various natural[1] and industrial contexts, including nanoparticle growth,[2] cloud formation,[3] frosting,[4] and dew formation.[5] A critical yet underexplored application of heterogeneous condensation with significant health implications is the nucleation and growth of liquid films on airborne viral particles. These liquid droplets enclosing viruses can undergo significant growth in environments with high humidity, such as in tropical climates, at high altitudes, fog,[6] inside respiratory tract,[7] and inside condensation-based growth tubes[8] and particle counters.[2] The condensation mechanisms play a crucial role in virion transport in the atmosphere and collection devices.[9,10] Viruses, typically classified as enveloped or nonenveloped, may feature diverse nanostructured surfaces. Nonenveloped viruses are generally enclosed by capsid proteins and have relatively uniform surface roughness,[11,12] whereas enveloped viruses, characterized by lipid bilayers with envelope proteins like glycoproteins, feature a wide range of surface topologies.[13]

Imaging techniques, such as cryo-EM tomography, X-ray crystallography, electron tomography, etc., have provided insights into the structural characteristics of various viruses, highlighting differences in viral diameter, glycoprotein (GP) sizes, shapes, and distributions. The diameters of Simian immunodeficiency virus (SIV) and human immunodeficiency virus (HIV-1) are 109 ± 14 and 100 ± 8 nm, respectively.[14] SIV virions have 73 ± 25 uniformly distributed envelope spikes with an average interspike distance of ≈15 nm, while HIV-1 virions have an average of 14 ± 7 envelope spikes without a periodic distance.[14] Their glycoproteins have an average height of 13.7 nm, and the diameter of the head is 10.5 nm.[14] SARS-CoV-1 and SARS-CoV-2 virions have diameters ranging from approximately 50 to 200 nm.[15] The spike proteins on these virions have heights between 9 and 12 nm, with a center-to-center distance of 22 nm and a diameter of 12−13 nm.[16−18]

Received: January 24, 2025
Revised: April 7, 2025
Accepted: April 14, 2025
Published: May 3, 2025

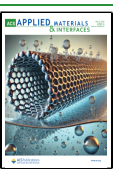

The Ebola virus exhibits a filamentous morphology with glycoprotein spikes of approximately 13 nm in height, a head diameter of 18 nm, and a stalk length and diameter of 5 and 3.5 nm, respectively.[19] Influenza A viral particles have an average diameter of 120 nm, with hemagglutinin (HA) glycoproteins measuring about 13−14 nm in height and 8 nm in diameter, and neuraminidase (NA) glycoproteins measuring 14−16 nm in height.[20−23] Respiratory syncytial virus (RSV) particles are filamentous, with diameters of ∼130 nm and lengths ranging from 500 nm to 12 μm, and feature a dense layer of fusion glycoproteins (F) and attachment glycoproteins (G) having heights ranging from 11.9 to 16.7 nm and a diameter of ∼10 nm.[24−26] The measles virus, with diameters of about 100−200 nm, has HA and F glycoproteins.[27] Mumps viral particles range from 100 to 600 nm in diameter and have hemagglutinin−neuraminidase (HN) and F glycoproteins.[28,29] Parainfluenza viruses have diameters of 150−200 nm with HN and F proteins.[30]

The wettability of viral surfaces and glycoproteins may play a key role in the viral condensation behavior and stability. The SARS-CoV-2 spike glycoprotein has hydrophilic regions for environmental interaction and hydrophobic regions for membrane fusion.[18] Influenza virus HA shows similar characteristics, with hydrophilic receptor-binding domains and hydrophobic entry regions.[31] HIV's glycosylated glycoprotein 120 (gp120) is hydrophilic, while glycoprotein 41 (gp41) contains hydrophobic regions essential for fusion.[14] Ebola virus glycoproteins feature hydrophilic mucin-like domains and hydrophobic fusion regions.[32] RSV's F and G glycoproteins also combine hydrophilic attachment sites with hydrophobic fusion domains.[33] MERS-CoV's spike glycoprotein[34] and the rhinovirus[35] (common cold virus) exhibit similar patterns.

In summary, viral surface geometry and interaction energy can vary significantly based on their glycoproteins' size, shape, density, and surface wettability. Therefore, fundamental insight into the role of surface characteristics in heterogeneous condensation and liquid film growth is necessary to fully understand the transport phenomena of these viruses.

While condensation on viral and bacterial particles has not received significant attention, extensive research has been conducted on condensation enhancement on various small-scale structured and unstructured surfaces.[36−39] These studies include condensation on chemically treated surfaces, surfaces with topology-based control, and condensation on whole particles. Toxvaerd et al. used molecular dynamics (MD) simulations to model homogeneous[40] and heterogeneous nucleation[41] of water vapor on unstructured solid surfaces. Sheng et al.[42] further characterized different modes of surface condensation using MD simulations. Others have investigated condensation on unstructured Mica (001) surfaces[43] and the effect of noncondensable gases[44] and electric fields.[45]

In addition to unstructured surfaces, the effect of surface modifications on condensation has also been computationally investigated. Chemically treating surfaces to alter various properties, such as the surface free energy[46] and surface wettability,[47,48] has been modeled through changes in the interaction of the surface atoms with water atoms. The parameters of the interatomic Lennard-Jones (L-J) potential, specifically the well depth of the potential (ε) and the distance where the L-J potential becomes zero (σ), are modified to achieve the desired wettability. Combinations of modified hydrophobic and hydrophilic surfaces have been utilized to enhance surface condensation.[49,50]

Topology-based control through the introduction of nanostructures has also been extensively studied. Various nanostructures, such as cuboidal,[51] cylindrical,[39] nano-grooved,[52] nanodimpled,[53] curved,[54] rough surfaces,[55] surfaces with varying solid fractions,[56] and a combination of modified surfaces and nanostructures,[39] have been used to control condensation. Furthermore, atomistic simulations have been used to model condensation on entire particles, including spherical[57] and cubic particles,[58] nanotubes,[59] nanorods,[60] and inside polymer networks.[61] Despite these advances, these studies do not address the influence of intricate surface structures found on viral and bacterial envelopes on condensation. A fundamental understanding of heterogeneous condensation on biothreat-like surfaces is crucial for predicting their transport in condensation-based capture devices and addressing a significant gap in understanding the airborne transport of viruses and bacteria.

Herein, we report the influence of viral envelope geometric parameters [pitch-to-diameter ratio (p/d)] and surface wettability on heterogeneous condensation. Three levels of surface wettability are considered: very hydrophilic (contact angle of θ = 15°, corresponding to an interaction intensity of f = 3.0), hydrophilic (θ = 75°, f = 2.0), and hydrophobic (θ = 105°, f = 1.5). Pitch-to-diameter ratios of p/d = 1.0, 1.2, 1.3, 1.7, 2.0, and ∞ were used, where p/d = 1.0 and ∞ represent an unstructured surface. Water molecule condensation on modeled surfaces was simulated to investigate the impact of surface topology and wettability on the normalized condensation rates and the normalized active surface area. The simulation results show that the condensation rates are heavily influenced by the surface parameters, which can vary significantly between the viral particles.

RESULTS AND DISCUSSION

Figure 1a shows the surface topology of a representative SARS-CoV-2 particle, which features glycoprotein structures on the viral envelope. In this study, we model this as a cylindrical pillar structure on a flat surface with uniform hydrophilicity. Figure 1b summarizes the general trend of the condensation rate on the simplified viral glycoprotein versus time. The features of the plot may vary across different cases, and all features may not be observed in every case. Initially, the condensation rate increases quickly due to the high surface

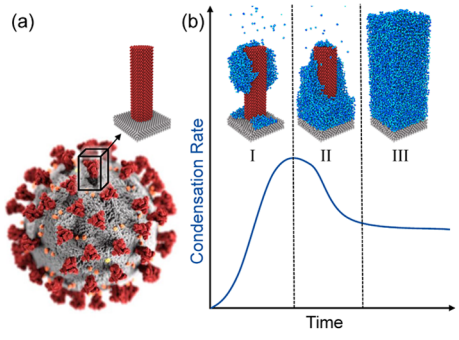

Figure 1. (a) Representative SARS-CoV-2 viral particle and the simplified viral glycoprotein structure modeled herein as a cylindrical pillar on a flat surface. (b) Generalized trend for the condensation rate versus time.

https://doi.org/10.1021/acsami.5c01789
ACS Appl. Mater. Interfaces 2025, 17, 27829−27838

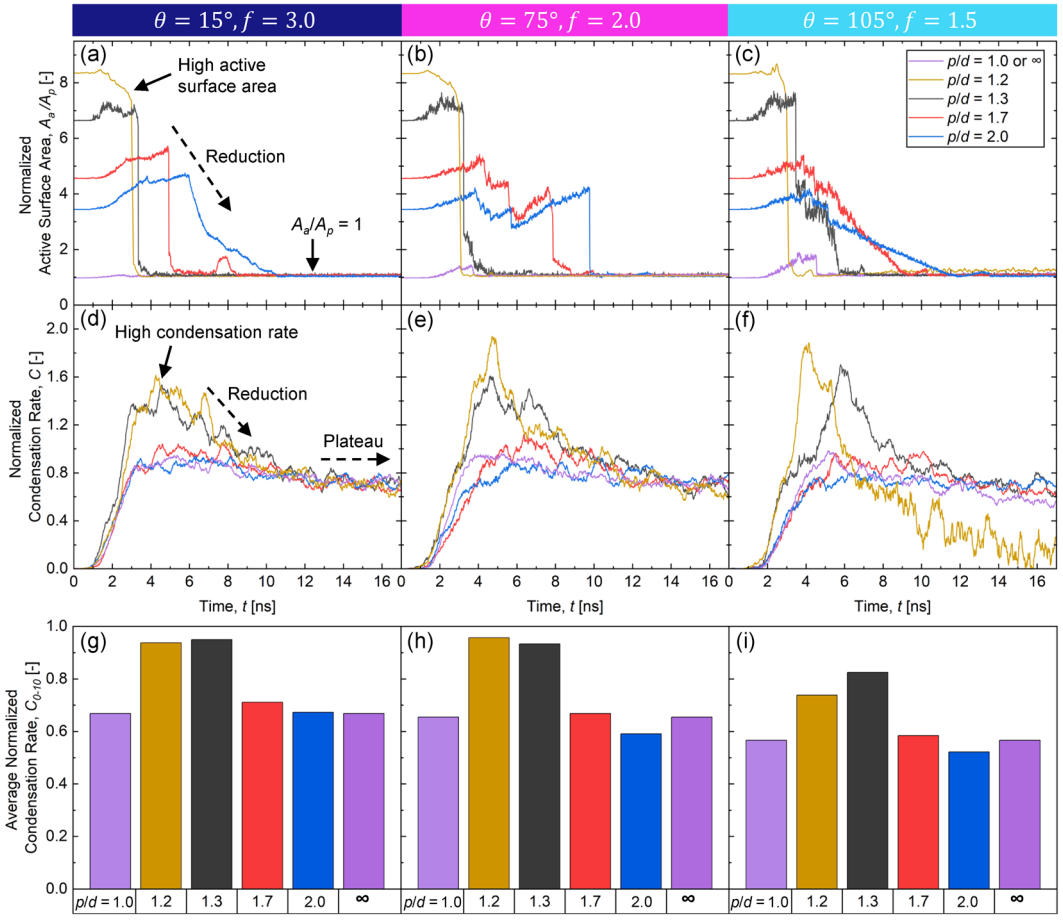

Figure 2. Effect of pitch-to-diameter ratio (p/d) on the normalized active surface area (a–c), normalized condensation rate (d–f), and average normalized condensation rates for the first 10 ns (g–i) for contact angles of $\theta = 15°$ ($f = 3.0$), 75° ($f = 2.0$), and 105° ($f = 1.5$), respectively. The colors corresponding to various pitch-to-diameter ratios shown in the legend in Figure 2c apply to the entire figure (i.e., a–i).

area of the solid surface, which serves as the condensation nucleation surface [region I in Figure 1b]. Shortly after nucleation, there is an increase in the active surface area [vapor–solid and vapor–liquid interfacial area (A_a)] due to initial cluster formation since the nonplanar vapor–liquid interface of the liquid clusters increases the active surface area. Shortly thereafter, the time rate of change in the condensation rate becomes negative [near the middle of region I of Figure 1b], which causes the increasing condensation rate to slow down and reach a maximum value. This is caused by liquid droplet coalescence, resulting in a decrease in the active surface area. As the clusters continue to coalesce, the solid surface becomes covered in liquid, gradually decreasing the active surface area and thus the condensation rate, as illustrated in region II in Figure 1b. Once the volume between the simplified glycoproteins is completely filled with liquid and no solid viral surface is exposed to vapor, the active surface area becomes constant and approaches the projected surface area [i.e., the unstructured surface area (A_p)]. At this point, the condensation rate approaches that of a plateau but has a slight negative slope, as shown in region III in Figure 1b. This negative slope is attributed to the continuously increasing thermal resistance between the solid and the vapor due to the increasing number of layers (i.e., thickness) of condensed water molecules.[62]

Figure 2 shows the results of the condensation simulations on simplified glycoprotein structures modeled as cylindrical pillars with varying pitch-to-diameter ratios (p/d) and different contact angles (θ). The figure illustrates the evolution of the normalized active surface area (A_a/A_p) and the normalized condensation rate (C) over time, as well as the average normalized condensation rate (C_{0-10}) from 0 to 10 s for different p/d ratios and contact angles. The active surface area (A_a) was normalized by dividing it by the projected surface area (A_p). Similarly, the condensation rate was normalized by dividing it by the peak (maximum) condensation rate of the unstructured surface for a contact angle of $\theta = 15°$. Due to the structured surface, the initial (i.e., at $t = 0$) normalized active surface area is greater than one, and this initial value increases as p/d decreases. Shortly after the simulation begins, the normalized active surface area increases due to the convex vapor–liquid interface that forms the clusters of condensed water molecules (Figure 2a–c and Figure S1 in the Supporting Information). The increase in active surface area (relative to the initial area) is more pronounced for surfaces with larger p/d ratios (e.g., $p/d = 1.7$ and 2.0) since these surfaces have more space for cluster formation between pillars, which then leads to increases in active surface area. Surfaces with smaller p/d ratios (e.g., $p/d = 1.2$ and 1.3) have less pillar-to-pillar distance, which facilitates water molecules bridging between pillars and creates vapor pockets under the liquid bridges and above the solid surface. This bridging prevents vapor molecules from reaching the bottom of the pillars, which rapidly reduces the normalized active surface area and subsequently reduces the

https://doi.org/10.1021/acsami.5c01789
ACS Appl. Mater. Interfaces 2025, 17, 27829–27838

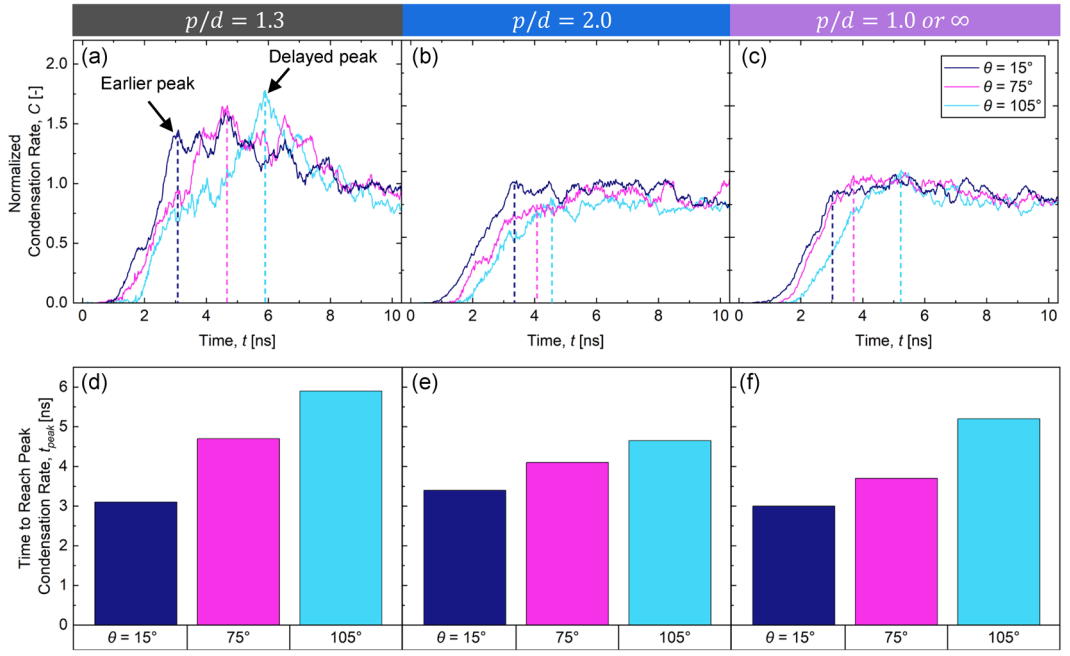

Figure 3. Effect of contact angle (interaction intensity) on normalized condensation rate for (a) p/d = 1.3, (b) p/d = 2.0, and (c) p/d = 1.0 or ∞. Comparison for the time to reach the peak condensation rate for contact angles (interaction intensities) of θ = 15°, 75°, and 105° for (d) p/d = 1.3, (e) p/d = 2.0, and (f) p/d = 1.0 or ∞.

condensation rate, as shown in Figure 2a–f, in Supporting Videos 1–15, and in Figure S1 in the Supporting Information. As time progresses, the liquid clusters coalesce, causing the normalized active surface area to decrease and approach unity as the condensation rate approaches the rate of an unstructured surface (as shown in region III in Figure 1). This trend is observed for all surfaces, regardless of the contact angle, although the initial increase and subsequent decline of the normalized active surface area vary in magnitude. The normalized condensation rate shows two different trends as time progresses, depending on the pitch-to-diameter ratio (p/d) [Figure 2d–f]. For intermediate ratios of p/d = 1.2–1.3, which feature an initial normalized surface area greater than six [Figure 2a–c], a larger normalized condensation rate [Figure 2d–f] is observed during the first approximately 10 ns irrespective of the contact angle compared to unstructured (p/d = 1.0 or ∞) or high pitch-to-diameter ratio ($p/d \geq 1.7$) surfaces. After the peak normalized condensation rate of approximately 1.6–2.0 is achieved for p/d = 1.2 and 1.3 at approximately 4–6 ns, a gradual decline is observed, and the condensation rates approach the plateau at $C \approx 0.8$ observed for all other surfaces after approximately 5 ns. This 2–3× enhancement indicates favorable condensation conditions for surfaces with intermediate p/d ratios. This indicates that biothreats with these intermediate spike protein densities (p/d = 1.2–1.3) may demonstrate enhanced particle capture efficiency due to rapid growth in a bioaerosol capture device.

For unstructured and $p/d \geq 1.7$ surfaces, which feature initial active surface area ratios less than five, a peak in the condensation rate is not observed. Instead, a gradual increase and subsequent plateau in the condensation rate to $C \approx 0.8$ is observed. The one exception to this is for θ = 105° and p/d = 1.2, which shows the normalized condensation rate rapidly drops to ≈ 0.2 after the large initial peak is observed at $t \approx 4$ ns [Figure 2f]. This rapid drop is caused by a Wenzel-to-Cassie state transition that occurs at $t \approx 4$ ns (Supporting Video 16). This transition is attributed to the combination of densely packed surface structures (i.e., p/D = 1.2) and the hydrophobic surface (i.e., θ = 105°). In the Cassie–Baxter state,[63] water clusters experience limited surface contact and rest on top of the surface structures. After the transition, the vapor condenses on an effectively very thick layer of water (due to the added pillar height). This increases the thermal resistance, resulting in a decreased condensation rate. It is worth noting that the Wenzel-to-Cassie state transition could have important implications because it may have the potential to induce other interesting phenomena, such as jumping droplets,[36] which could significantly alter the condensation processes. These phenomena can be explored in future work.

The enhancement in the normalized condensation rate for intermediate p/d ratios is illustrated in Figure 2g–i, which shows the average normalized condensation rate during the first 10 ns (after which all of the condensation rates are identical). The maximum average condensation rate is observed for p/d = 1.2 and 1.3, regardless of the contact angle (interaction intensity). These results suggest that the glycoprotein distance on the viral particle significantly impacts the condensation mechanisms and rates. It is also widely reported that flat (unstructured) hydrophilic surfaces tend to exhibit higher condensation rates.[41,46,47] A similar trend is observed in our simulations for both structured and unstructured (flat) surfaces. As shown in Figure 2g–i, the average normalized condensation rate is lower for θ = 105° compared to θ = 15° and 75°, regardless of the pitch-to-diameter ratio.

The obtained results can be broadly applied because the range of pitch-to-diameter ratios used herein ($1 \leq p/d \leq 2$) spans those of common viruses. For instance, the estimated p/d ratios for RSV, Influenza, SIV, and SARS-CoV-2 are approximately 1, 1.3, 1.43, and 1.69, respectively.[14–18,20–26] This suggests that Influenza and SIV are likely to exhibit higher initial condensation rates, while RSV and SARS-CoV-2 may

https://doi.org/10.1021/acsami.5c01789
ACS Appl. Mater. Interfaces 2025, 17, 27829–27838

experience condensation behavior similar to that of a structureless surface. Moreover, viruses that are more hydrophobic will likely feature reduced condensation rates compared to those that are more hydrophilic.

Figure 3 illustrates the effect of the contact angle (θ) on the normalized condensation rate for three pitch-to-diameter ratios (p/d). Figure 3a–c shows the time-resolved normalized condensation rate (C), and Figure 3d–f shows the time to reach the peak normalized condensation rate (t_{peak}) for different contact angles and pitch-to-diameter ratios, as indicated by the dashed vertical line in Figure 3a–c. The effect of contact angle (interaction intensity) is only visible until all of the surface area is fully covered by water molecules, as shown in Supporting Videos 1–15 and Figure S2 in the Supporting Information. As shown in Figure 3a–c (from $t \approx$ 0–2 ns), nucleation begins sooner for more hydrophilic surfaces (e.g., θ = 15°), regardless of the p/d ratio, because they have more affinity to water molecules (i.e., are more hydrophilic). This earlier nucleation can be attributed to the lower energy barrier for water molecule adsorption on hydrophilic surfaces.[46,64,65] Similarly, the peak condensation rate is achieved more quickly for more hydrophilic surfaces, affirming the higher initial condensation rate. This suggests that viral or bacterial particles with hydrophilic glycoproteins will exhibit earlier and faster condensation compared to those with hydrophobic surfaces. For p/d = 1.3, large, distinct peaks in the normalized condensation rate with subsequent gradual decline that plateaus out at $C \approx 1$ are visible. In contrast, for p/d = 2.0 and p/d = 1.0 or ∞, the normalized condensation rate profiles increase monotonically (i.e., do not peak and then reduce) before plateauing out at $C \approx 1$. Moreover, for p/d = 2.0 and p/d = 1.0 or ∞, the three curves are more similar to each other than those for p/d = 1.3. This uniformity suggests that the contact angle (which corresponds to the three different lines) has less influence on the condensation process for p/d = 2.0 and p/d = 1.0 or ∞ than it does for p/d = 1.3. Figure 3d–f compares the time to reach the peak condensation rate for different contact angles and for each pitch-to-diameter ratio. It is observed that the t_{peak} increases as the contact angle increases because the weaker interaction between water molecules and surface atoms (i.e., smaller interaction intensity, which results in a larger contact angle) slows down the condensation process. This trend is consistent across all p/d ratios, emphasizing the critical role of surface wettability in condensation dynamics on glycoprotein-covered viral particles.

CONCLUSIONS

This study provides detailed insights into the relatively unexplored and intricate dynamics of heterogeneous condensation on simplified viral and bacterial envelopes. Since condensation-based growth can significantly increase the mass of bioaerosols and thus reduce the suspension/settling/residence time of the biothreat in the air, this study aids the understanding of airborne biothreat transport phenomena in various applications, such as the atmosphere, respiratory tract, and condensation-based capture devices. By exploring the surface topological parameters, such as the normalized pitch-to-diameter ratio (p/d) and surface wettability using MD simulations, we showed that there is a strong correlation between these parameters and condensation rate and active surface area. These interactions govern the particle growth during the condensation process, which thereby affects transport phenomena. The simplified viral surface topologies used in this study enable the results to be applied to a variety of viruses and other microorganisms that feature a wide range of protein structure arrangements. With continual increases in computational power and advanced modeling capabilities, future research can model complex and specific viral envelope structures to obtain application-specific condensation and transport behavior. Additionally, investigating the effects of varying aspect ratios, whether by altering pillar height or spacing, could provide deeper insights into how diffusion length scales influence condensation dynamics. Furthermore, studying condensation on viral envelopes under dynamic conditions, mixed surface wettability, or external fields (e.g., electric fields) could provide a valuable understanding of specific cases.

METHODOLOGY

The heterogeneous condensation of water molecules on simplified viral envelopes was simulated using the Large-scale Atomic/Molecular Massively Parallel Simulator (LAMMPS).[66] A cuboidal simulation domain was utilized with periodic boundary conditions on all sides, as illustrated in Figure 4. A single glycoprotein structure, approximated as a cylindrical pillar with a height of 10 nm and a diameter of 3 nm, was used in the simulations. The pitch (i.e., the center-to-center distance between pillars) was varied for each of the cases for various pitch-to-diameter ratios (p/d) (1.0, 1.2, 1.3, 1.7, 2.0, and ∞). This range was chosen such that it encompasses the pitch-to-diameter ratios observed in common viruses, such as SARS-CoV-2, SIV, HIV, Influenza, and RSV, which are generally between one and two.[14–18,20–26] The height of the simulation domain was set to 64 nm in the z-direction, more than six times the pillar height, to eliminate the possibility of any boundary-related effects in that direction. The dimensions along the x- and y-axes were determined from the pitch and pillar diameter. Given that the size of a viral particle can be approximated as a 60–300 nm sphere, as discussed before, the

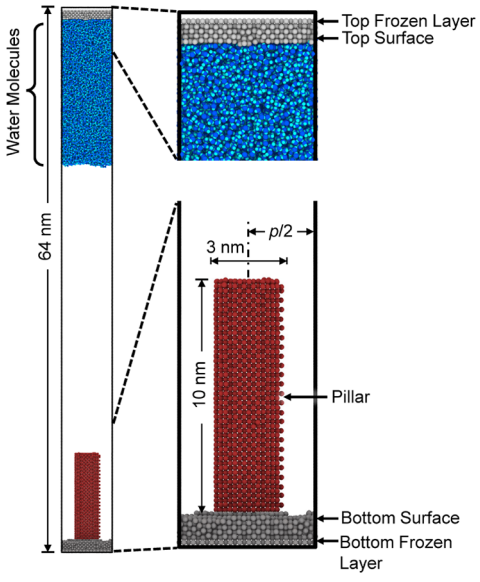

Figure 4. Simulation domain with periodic boundary conditions is used to investigate heterogeneous condensation of water (blue) on a simplified glycoprotein-viral envelope, modeled as a cylindrical pillar (red) on a flat surface (gray). The height and diameter of the pillar are 10 and 3 nm, respectively.

https://doi.org/10.1021/acsami.5c01789
ACS Appl. Mater. Interfaces 2025, 17, 27829–27838

curvature effect of the surface that the pillar is attached to was disregarded, treating the unit cell around a single glycoprotein on the viral envelope as a flat surface. The simulation domain consists of the bottom surface, a cylindrical pillar, which represents the simplified glycoprotein structure, the top surface, and water molecules adjacent to the top surface. The simplified glycoprotein structure and flat surfaces were formed by adding Au molecules in a face-centered cubic (FCC) structure with a lattice constant of 4.08 Å. The top and bottom surfaces consist of six layers of atoms, including one frozen layer on the uppermost and lowermost positions, respectively (Figure 4), to maintain their shapes, and were kept in place using the Embedded Atom Potential (EAM) force field.[67] The simplified glycoprotein structure consists of a 'frozen' cylinder with a diameter of 2 nm and a height of 9.6 nm in the core, surrounded by Au atoms to form the cylindrical pillar. Although the EAM potential is often used for modeling metals, the purpose of using it here was to form the structure. The interaction between the surface atoms and water molecules was modified to achieve a range of contact angles. The water molecules were modeled using the extended simple point charge (SPC/E) water model,[68] which has been proven to be reliable for modeling phase change phenomena and can accurately predict liquid−vapor interfacial tension.[69]

For each simulation, a single pillar with the desired pitch was simulated as opposed to employing multiple pillar structures, given the utilization of periodic boundary conditions. Notably, simulations featuring a single unit cell (with one pillar) and multiple pillars yielded essentially identical results, as illustrated in Figure S3 in the Supporting Information.

The interaction between water molecules and the interaction between water molecules and Au atoms were modeled using the 12−6 L-J and Coulombic potentials with a cutoff distance of 10 Å. The atomic potential is given by

$$U_{ij} = 4\varepsilon\left[\left(\frac{\sigma_{ij}}{r_{ij}}\right)^{12} - \left(\frac{\sigma_{ij}}{r_{ij}}\right)^{6}\right] + \frac{1}{4\pi\varepsilon_o}\frac{q_i q_j}{r_{ij}} \quad (1)$$

where ε_{ij} represents the depth of the potential well between atom i and atom j; σ_{ij} is the distance between atom i and atom j, where the interparticle potential is zero; r_{ij} is the distance between atom i and atom j; q_i and q_j are the electric charges of atoms i and j, respectively; and ε_o is the permittivity of the vacuum. The particle−particle particle−mesh (PPPM) method was used for the Coulombic long-range interaction. The SHAKE algorithm[70] was used to constrain the bond and angle in the water molecules.

Determining the pair potential for the viral envelope is challenging due to its high nonuniformity. The viral envelope differs from virus to virus, even within the same virus family. In general, the viral envelope surface consists of a lipid bilayer, which is predominantly hydrophilic,[71] with reported contact angles typically less than 60°.[72] While the constituent amino acids of the envelope glycoprotein can exhibit specific hydrophobic or hydrophilic properties in their monomer,[73] determining the overall surface wettability of a protein structure poses significant difficulty because it comprises multiple amino acids and forms a complex chain with distinct topologies. The limited data available on the surface wettability of these proteins suggests the final glycoprotein structure can be hydrophilic, hydrophobic, or a combination of hydrophilic−hydrophobic spots.[74] In MD simulations, the wettability of the surface can be controlled by tuning the depth of the L-J potential well between oxygen and Au (ε_{O-Au}).[46] For simplicity, the depth of the LJ potential well between oxygen and Au (ε_{O-Au}) was kept constant across the entire bottom surface and pillar in each simulation. The influence of the contact angle (i.e., surface wettability) was investigated by varying the interaction intensity (f), which is the ratio of the depth of the LJ potential well for surface atoms to oxygen atoms ($\varepsilon_{O-Au}/\varepsilon_{O-O}$). Herein, ε_{O-O} = 0.0067 eV[68] is held constant, while the depth of the LJ potential well between Au and oxygen atoms is varied, with ε_{O-Au} = 0.01005, 0.13400, and 0.02010 eV, resulting in interaction intensities of f = 1.5, 2.0, 3.0, respectively, which correspond to constant angles of θ = 105°, 75°, and 15°, respectively.[44] Thus, the contact angles range from hydrophobic to hydrophilic surfaces. The potential energy parameters used in the simulations are shown in Table 1. The hydrogen−oxygen interaction parameters are determined by the Lorentz−Berthelot mixing rules[75] using

$$\sigma_{ij} = \frac{\sigma_{ii} + \sigma_{jj}}{2} \quad (2)$$

$$\varepsilon_{ij} = \sqrt{\varepsilon_{ii}\varepsilon_{jj}} \quad (3)$$

It is crucial to introduce the correct number of water molecules in the simulation to prevent unrealistic system behavior. This can be achieved by either calculating and introducing the exact number of water molecules required to achieve a particular saturation pressure at a given temperature[46,48] or by boiling water inside the domain and allowing the water to vaporize as needed based on the system's saturation level.[39,53] While the former approach is computationally less intensive, the latter method offers a more stable saturation profile. Therefore, the latter approach was used.

The simulation comprised two stages. First, the entire system was allowed to achieve equilibration at 298 K using a Nose−Hoover thermostat in the NVT [constant moles (N), volume (V), and temperature (T)] ensemble. This was achieved within 1 ns. In the second stage, the thermostats were removed, the NVE [constant moles (N), volume (V), and energy (E)] ensemble was imposed, and the top surface temperature was set to 500 K using the Langevin thermostat. The beginning of the second stage is defined as t = 0 ns in all figures. A time step of 2 fs was used for the simulation, which was validated by comparing the results obtained using various time step sizes, as shown in the Supporting Information (Figure S4). OVITO[76] software was used for the visualization of atomic interactions, the analysis of clusters using the Stillinger criterion[77] with a cutoff distance of 3.36 Å between two oxygen atoms, and the evaluation of the active surface area. MATLAB scripts were used to analyze the raw data and analyze the temperature, energy, and pressure data, as described in the Supporting Information (Figure S5).

Table 1. Potential Energy Parameters Used in the MD Simulations[67,68]

atoms i−j	$q(e)$	σ_{ij} (Å)	ε_{ij} (eV)
H−H	+0.4238	0	0
O−O	−0.8476	3.16600	0.006700
H−Au		0	0
O−Au (top surface)		2.86750	0.02010
O−Au (bottom surface)		2.86750	0.01005−0.02010

https://doi.org/10.1021/acsami.5c01789
ACS Appl. Mater. Interfaces 2025, 17, 27829−27838

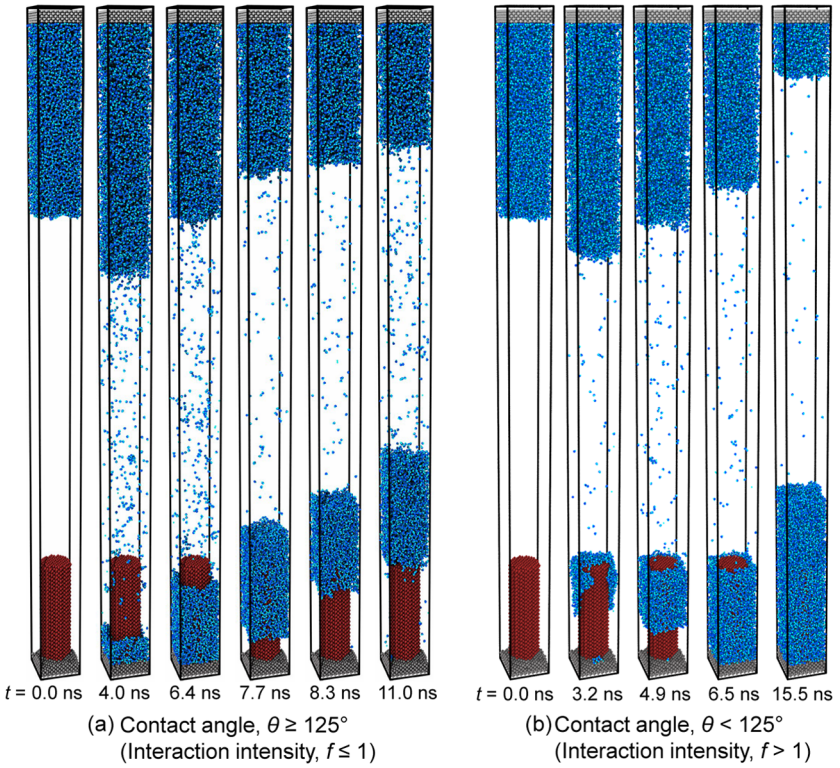

Figure 5. Visualization of the transient evolution of condensation on (a) very hydrophobic surface ($\theta \geq 125°$, $f \leq 1$) and (b) hydrophobic-to-hydrophilic surface ($\theta < 125°$, $f > 1$). The Wenzel-to-Cassie state transition that often occurs on hydrophobic surfaces during condensation is illustrated in panel (a) and shown in Supporting Video 16.

Our rationale for the selection of the range of contact angles used in this study is illustrated in Figure 5. Surfaces with contact angles greater than 125°, which indicate moderate-to-high hydrophobicity, often exhibit a Wenzel-to-Cassie state transition,[78] as illustrated in Figure 5a and Supporting Video 16 and as reported by others.[39,46,56,79] This behavior was observed in this study for $\theta = 105°$ and $p/d = 1.2$ and for all cases with $\theta > 125$. Because condensation in the Cassie–Baxter state resembled that of condensation on a flat surface (as previously described), we limited our investigation to surfaces with contact angles <125°.

■ ASSOCIATED CONTENT

Supporting Information

The Supporting Information is available free of charge at https://pubs.acs.org/doi/10.1021/acsami.5c01789.

Additional analysis on water molecule bridging and vapor pocket formation, effect of contact angle on pillar coverage, effect of the number of pillars, size of the time step, and temperature and energy profiles (PDF)

Time-resolved evolution of the normalized active surface area, normalized condensation rate, and visualization of the condensation process in the simulation domain for $p/d = 1.0$ or ∞ and $\theta = 15°$ (MP4)

Time-resolved evolution of the normalized active surface area, normalized condensation rate, and visualization of the condensation process in the simulation domain for $p/d = 1.2$ and $\theta = 15°$ (MP4)

Time-resolved evolution of the normalized active surface area, normalized condensation rate, and visualization of the condensation process in the simulation domain for $p/d = 1.3$ and $\theta = 15°$ (MP4)

Time-resolved evolution of the normalized active surface area, normalized condensation rate, and visualization of the condensation process in the simulation domain for $p/d = 1.7$ and $\theta = 15°$ (MP4)

Time-resolved evolution of the normalized active surface area, normalized condensation rate, and visualization of the condensation process in the simulation domain for $p/d = 2.0$ and $\theta = 15°$ (MP4)

Time-resolved evolution of the normalized active surface area, normalized condensation rate, and visualization of the condensation process in the simulation domain for $p/d = 1.0$ or ∞ and $\theta = 75°$ (MP4)

Time-resolved evolution of the normalized active surface area, normalized condensation rate, and visualization of the condensation process in the simulation domain for $p/d = 1.2$ and $\theta = 75°$ (MP4)

Time-resolved evolution of the normalized active surface area, normalized condensation rate, and visualization of the condensation process in the simulation domain for $p/d = 1.3$ and $\theta = 75°$ (MP4)

Time-resolved evolution of the normalized active surface area, normalized condensation rate, and visualization of the condensation process in the simulation domain for $p/d = 1.7$ and $\theta = 75°$ (MP4)

Time-resolved evolution of the normalized active surface area, normalized condensation rate, and visualization of the condensation process in the simulation domain for $p/d = 2.0$ and $\theta = 75°$ (MP4)

Time-resolved evolution of the normalized active surface area, normalized condensation rate, and visualization of the condensation process in the simulation domain for $p/d = 1.0$ or ∞ and $\theta = 105°$ (MP4)

https://doi.org/10.1021/acsami.5c01789
ACS Appl. Mater. Interfaces 2025, 17, 27829−27838

Time-resolved evolution of the normalized active surface area, normalized condensation rate, and visualization of the condensation process in the simulation domain for p/d = 1.2 and θ = 105° (MP4)

Time-resolved evolution of the normalized active surface area, normalized condensation rate, and visualization of the condensation process in the simulation domain for p/d = 1.3 and θ = 105° (MP4)

Time-resolved evolution of the normalized active surface area, normalized condensation rate, and visualization of the condensation process in the simulation domain for p/d = 1.7 and θ = 105° (MP4)

Time-resolved evolution of the normalized active surface area, normalized condensation rate, and visualization of the condensation process in the simulation domain for p/d = 2.0 and θ = 105° (MP4)

Visualization of the Wenzel-to-Cassie state transition (MP4)

AUTHOR INFORMATION

Corresponding Author

Todd A. Kingston − *Center for Multiphase Flow Research and Education, Department of Mechanical Engineering, Iowa State University, Ames, Iowa 50011, United States;* orcid.org/0000-0003-4981-4884; Email: kingston@iastate.edu

Authors

Kawkab Ahasan − *Center for Multiphase Flow Research and Education, Department of Mechanical Engineering, Iowa State University, Ames, Iowa 50011, United States*

Han Hu − *Department of Mechanical Engineering, University of Arkansas, Fayetteville, Arkansas 72701, United States;* orcid.org/0000-0002-9667-1698

Pranav Shrotriya − *Center for Multiphase Flow Research and Education, Department of Mechanical Engineering, Iowa State University, Ames, Iowa 50011, United States;* orcid.org/0000-0001-9263-4892

Complete contact information is available at: https://pubs.acs.org/10.1021/acsami.5c01789

Notes

The authors declare no competing financial interest.

ACKNOWLEDGMENTS

We gratefully acknowledge the Department of Homeland Security (DHS) for funding this work (Cooperative Agreement: 20CWDARI00033). We appreciate critical discussion and suggestions from our many collaborators, including Marit Nilsen-Hamilton, Wendy Maury, Monica Lamm, Lee Bendickson, Michael Murphy, Sam De Penning, Anthony David, and Sadiqul Islam. The computing support for the research reported in this paper was supported, in part, by two National Science Foundation grants, MRI1726447 and MRI2018594. This research was also funded, in part, by the Philip and Virginia Sproul Professorship at Iowa State University and the Iowa State University Presidential Interdisciplinary Research Seed grant.

NOMENCLATURE

A_a	active surface area
A_p	projected surface area
C	normalized condensation rate
C_{0-10}	average normalized condensation rate from 0 to 10 ns
d	pillar diameter
f	interaction intensity
p	pitch (i.e., center-to-center distance between pillars)
q_i and q_j	electric charges of atoms i and j
r_{ij}	distance between atom i and j
t_{peak}	time to reach the peak condensation rate
U_{ij}	Lennard-Jones (L-J) potential between i and j atoms

Greek letters

ε_o	permittivity of the vacuum
ε_{ij}	depth of the L-J potential well between i and j atoms
ε_{O-O}	depth of the L-J potential well between two oxygen atoms
ε_{O-Au}	depth of the L-J potential well between oxygen and gold (surface) atoms
ε_{Au-Au}	depth of the L-J potential well between gold (surface) atoms
σ_{ij}	distance where the interparticle potential is zero for i and j atoms
θ	contact angle

REFERENCES

(1) Parker, A. R.; Lawrence, C. R. Water Capture by a Desert Beetle. *Nature* **2001**, *414* (6859), 33−34.

(2) McMurry, P. H. The History of Condensation Nucleus Counters. *Aerosol Sci. Technol.* **2000**, *33* (4), 297−322.

(3) Charlson, R. J.; Seinfeld, J. H.; Nenes, A.; Kulmala, M.; Laaksonen, A.; Facchini, M. C. Reshaping the Theory of Cloud Formation. *Science* **2001**, *292* (5524), 2025−2026.

(4) Nath, S.; Ahmadi, S. F.; Boreyko, J. B. A Review of Condensation Frosting. *Nanoscale Microscale Thermophys. Eng.* **2017**, *21* (2), 81−101.

(5) Beysens, D. The Formation of Dew. *Atmospheric Res.* **1995**, *39* (1), 215−237.

(6) Mazoyer, M.; Burnet, F.; Denjean, C. Experimental Study on the Evolution of Droplet Size Distribution during the Fog Life Cycle. *Atmospheric Chem. Phys.* **2022**, *22* (17), 11305−11321.

(7) Walker, J. E. C.; Wells, R. E. Heat and Water Exchange in the Respiratory Tract. *Am. J. Med.* **1961**, *30* (2), 259−267.

(8) Hering, S. V.; Stolzenburg, M. R. A Method for Particle Size Amplification by Water Condensation in a Laminar, Thermally Diffusive Flow. *Aerosol Sci. Technol.* **2005**, *39* (5), 428−436.

(9) Wang, L.; Qi, W.; Liu, Y.; Essien, D.; Zhang, Q.; Lin, J. Recent Advances on Bioaerosol Collection and Detection in Microfluidic Chips. *Anal. Chem.* **2021**, *93* (26), 9013−9022.

(10) Ahasan, K.; Schnoebelen, N. J.; Shrotriya, P.; Kingston, T. A. Continuous Sampling of Aerosolized Particles Using Stratified Two-Phase Microfluidics. *ACS Sens.* **2024**, *9*, 2915.

(11) Azad, K.; Banerjee, M. Structural Dynamics of Nonenveloped Virus Disassembly Intermediates. *J. Virol.* **2019**, *93* (22), No. e01115-19.

(12) Zhang, X.; Jin, L.; Fang, Q.; Hui, W. H.; Zhou, Z. H. 3.3 Å Cryo-EM Structure of a Nonenveloped Virus Reveals a Priming Mechanism for Cell Entry. *Cell* **2010**, *141* (3), 472−482.

(13) Gelderblom, H. R. *Structure and Classification of Viruses*. In Medical Microbiology; Baron, S., Ed.; University of Texas Medical Branch at Galveston: Galveston (TX), 1996.

(14) Zhu, P.; Liu, J.; Bess, J.; Chertova, E.; Lifson, J. D.; Grisé, H.; Ofek, G. A.; Taylor, K. A.; Roux, K. H. Distribution and Three-Dimensional Structure of AIDS Virus Envelope Spikes. *Nature* **2006**, *441* (7095), 847−852.

(15) Chatterjee, S. *Understanding the Nature of Variations in Structural Sequences Coding for Coronavirus Spike, Envelope, Membrane*

and Nucleocapsid Proteins of SARS-CoV-2. Rochester, NY, March 28, 2020. .
(16) Ke, Z.; Oton, J.; Qu, K.; Cortese, M.; Zila, V.; McKeane, L.; Nakane, T.; Zivanov, J.; Neufeldt, C. J.; Cerikan, B.; Lu, J. M.; Peukes, J.; Xiong, X.; Kräusslich, H.-G.; Scheres, S. H. W.; Bartenschlager, R.; Briggs, J. A. G. Structures and Distributions of SARS-CoV-2 Spike Proteins on Intact Virions. *Nature* **2020**, *588* (7838), 498−502.
(17) Taha, B. A.; Al-Jubouri, Q.; Al Mashhadany, Y.; Hafiz Mokhtar, M. H.; Bin Zan, M. S. D.; Bakar, A. A. A.; Arsad, N. Density Estimation of SARS-CoV2 Spike Proteins Using Super Pixels Segmentation Technique. *Appl. Soft Comput.* **2023**, *138*, No. 110210.
(18) Walls, A. C.; Park, Y.-J.; Tortorici, M. A.; Wall, A.; McGuire, A. T.; Veesler, D. Structure, Function, and Antigenicity of the SARS-CoV-2 Spike Glycoprotein. *Cell* **2020**, *181* (2), 281−292.e6.
(19) Beniac, D. R.; Booth, T. F. Structure of the Ebola Virus Glycoprotein Spike within the Virion Envelope at 11 Å Resolution. *Sci. Rep.* **2017**, *7* (1), 46374.
(20) Harris, A.; Cardone, G.; Winkler, D. C.; Heymann, J. B.; Brecher, M.; White, J. M.; Steven, A. C. Influenza Virus Pleiomorphy Characterized by Cryoelectron Tomography. *Proc. Natl. Acad. Sci. U. S. A.* **2006**, *103* (50), 19123−19127.
(21) Fontana, J.; Steven, A. C. Influenza Virus-Mediated Membrane Fusion: Structural Insights from Electron Microscopy. *Arch. Biochem. Biophys.* **2015**, *581*, 86−97.
(22) Wasilewski, S.; Calder, L. J.; Grant, T.; Rosenthal, P. B. Distribution of Surface Glycoproteins on Influenza A Virus Determined by Electron Cryotomography. *Vaccine* **2012**, *30* (51), 7368.
(23) Gamblin, S. J.; Haire, L. F.; Russell, R. J.; Stevens, D. J.; Xiao, B.; Ha, Y.; Vasisht, N.; Steinhauer, D. A.; Daniels, R. S.; Elliot, A.; Wiley, D. C.; Skehel, J. J. The Structure and Receptor Binding Properties of the 1918 Influenza Hemagglutinin. *Science* **2004**, *303* (5665), 1838−1842.
(24) Kiss, G.; Holl, J. M.; Williams, G. M.; Alonas, E.; Vanover, D.; Lifland, A. W.; Gudheti, M.; Guerrero-Ferreira, R. C.; Nair, V.; Yi, H.; Graham, B. S.; Santangelo, P. J.; Wright, E. R. Structural Analysis of Respiratory Syncytial Virus Reveals the Position of M2−1 between the Matrix Protein and the Ribonucleoprotein Complex. *J. Virol.* **2014**, *88* (13), 7602−7617.
(25) Battles, M. B.; McLellan, J. S. Respiratory Syncytial Virus Entry and How to Block It. *Nat. Rev. Microbiol.* **2019**, *17* (4), 233−245.
(26) Rossey, I.; Gilman, M. S. A.; Kabeche, S. C.; Sedeyn, K.; Wrapp, D.; Kanekiyo, M.; Chen, M.; Mas, V.; Spitaels, J.; Melero, J. A.; Graham, B. S.; Schepens, B.; McLellan, J. S.; Saelens, X. Potent Single-Domain Antibodies That Arrest Respiratory Syncytial Virus Fusion Protein in Its Prefusion State. *Nat. Commun.* **2017**, *8* (1), 14158.
(27) Colf, L. A.; Juo, Z. S.; Garcia, K. C. Structure of the Measles Virus Hemagglutinin. *Nat. Struct. Mol. Biol.* **2007**, *14* (12), 1227−1228.
(28) Frost, J. R.; Shaikh, S.; Severini, A. Exploring the Mumps Virus Glycoproteins: A Review. *Viruses* **2022**, *14* (6), 1335.
(29) Tang, S.; Kotra, L. P. *Mumps*. In xPharm: The Comprehensive Pharmacology Reference; Enna, S. J.; Bylund, D. B., Eds.; Elsevier: New York, 2007; pp 1−4. .
(30) Elboukari, H.; Ashraf, M. *Parainfluenza Virus*. In StatPearls; StatPearls Publishing: Treasure Island (FL), 2024.
(31) Gamblin, S. J.; Skehel, J. J. Influenza Hemagglutinin and Neuraminidase Membrane Glycoproteins*. *J. Biol. Chem.* **2010**, *285* (37), 28403−28409.
(32) Lee, J. E.; Fusco, M. L.; Hessell, A. J.; Oswald, W. B.; Burton, D. R.; Saphire, E. O. Structure of the Ebola Virus Glycoprotein Bound to an Antibody from a Human Survivor. *Nature* **2008**, *454* (7201), 177−182.
(33) McLellan, J. S.; Chen, M.; Leung, S.; Graepel, K. W.; Du, X.; Yang, Y.; Zhou, T.; Baxa, U.; Yasuda, E.; Beaumont, T.; Kumar, A.; Modjarrad, K.; Zheng, Z.; Zhao, M.; Xia, N.; Kwong, P. D.; Graham, B. S. Structure of RSV Fusion Glycoprotein Trimer Bound to a Prefusion-Specific Neutralizing Antibody. *Science* **2013**, *340* (6136), 1113−1117.
(34) Walls, A. C.; Xiong, X.; Park, Y.-J.; Tortorici, M. A.; Snijder, J.; Quispe, J.; Cameroni, E.; Gopal, R.; Dai, M.; Lanzavecchia, A.; Zambon, M.; Rey, F. A.; Corti, D.; Veesler, D. Unexpected Receptor Functional Mimicry Elucidates Activation of Coronavirus Fusion. *Cell* **2019**, *176* (5), 1026−1039.e15.
(35) Smith, T. J.; Kremer, M. J.; Luo, M.; Vriend, G.; Arnold, E.; Kamer, G.; Rossmann, M. G.; McKinlay, M. A.; Diana, G. D.; Otto, M. J. The Site of Attachment in Human Rhinovirus 14 for Antiviral Agents That Inhibit Uncoating. *Science* **1986**, *233* (4770), 1286−1293.
(36) Miljkovic, N.; Enright, R.; Nam, Y.; Lopez, K.; Dou, N.; Sack, J.; Wang, E. N. Jumping-Droplet-Enhanced Condensation on Scalable Superhydrophobic Nanostructured Surfaces. *Nano Lett.* **2013**, *13* (1), 179−187.
(37) Che, Q.; Wang, F.; Zhao, X. Design of Nanostructured Surfaces for Efficient Condensation by Controlling Condensation Modes. *Micromachines* **2023**, *14* (1), 50.
(38) Chen, L.; Wang, S.-Y.; Xiang, X.; Tao, W.-Q. Mechanism of Surface Nanostructure Changing Wettability: A Molecular Dynamics Simulation. *Comput. Mater. Sci.* **2020**, *171*, No. 109223.
(39) Dai, X.; Wang, M.; Zhang, J.; Xin, G.; Wang, X. Vapor Condensation on Bioinspired Hierarchical Nanostructured Surfaces with Hybrid Wettabilities. *Langmuir* **2022**, *38* (36), 11099−11108.
(40) Toxvaerd, S. Molecular-Dynamics Simulation of Homogeneous Nucleation in the Vapor Phase. *J. Chem. Phys.* **2001**, *115* (19), 8913−8920.
(41) Toxvaerd, S. Molecular Dynamics Simulation of Heterogeneous Nucleation at a Structureless Solid Surface. *J. Chem. Phys.* **2002**, *117* (22), 10303−10310.
(42) Sheng, Q.; Sun, J.; Wang, Q.; Wang, W.; Wang, H. S. On the Onset of Surface Condensation: Formation and Transition Mechanisms of Condensation Mode. *Sci. Rep.* **2016**, *6* (1), 30764.
(43) Ou, X.; Wang, X.; Lin, Z.; Li, J. Heterogeneous Condensation of Water on the Mica (001) Surface: A Molecular Dynamics Simulation Work. *J. Phys. Chem. C* **2017**, *121* (12), 6813−6819.
(44) Qiang, W.; Lan, Z.; Du, B.; Ren, W.; Xu, W.; Wen, R.; Ma, X. Enrichment Effects Induced by Non-Uniform Wettability Surfaces in the Presence of Non-Condensable Gas: A Molecular Dynamics Simulation. *Langmuir* **2022**, *38* (33), 10192−10201.
(45) Wang, P.; Min, B.; Wei, L.; Chen, X.; Wang, Z.; Chen, Z.; Li, S. Controlling the Condensation of Vapor by Electric Field: A Molecular Dynamics Simulation Study. *Appl. Surf. Sci.* **2022**, *605*, No. 154805.
(46) Xu, W.; Lan, Z.; Peng, B. L.; Wen, R. F.; Ma, X. H. Effect of Surface Free Energies on the Heterogeneous Nucleation of Water Droplet: A Molecular Dynamics Simulation Approach. *J. Chem. Phys.* **2015**, *142* (5), No. 054701.
(47) Niu, D.; Tang, G. H. The Effect of Surface Wettability on Water Vapor Condensation in Nanoscale. *Sci. Rep.* **2016**, *6* (1), 19192.
(48) Ranathunga, D. T. S.; Shamir, A.; Dai, X.; Nielsen, S. O. Molecular Dynamics Simulations of Water Condensation on Surfaces with Tunable Wettability. *Langmuir* **2020**, *36* (26), 7383−7391.
(49) Wang, Z.-J.; Wang, S.-Y.; Wang, D.-Q.; Yang, Y.-R.; Wang, X.-D.; Lee, D.-J. Water Vapor Condensation on Binary Mixed Substrates: A Molecular Dynamics Study. *Int. J. Heat Mass Transfer* **2022**, *184*, No. 122281.
(50) Wang, Z.-J.; Wang, S.-Y.; Wang, D.-Q.; Yang, Y.-R.; Wang, X.-D.; Lee, D.-J. Water Vapor Condensation on Substrates with Nanoscale Hydrophilic Spots: A Molecular Dynamics Study. *Int. J. Heat Mass Transfer* **2023**, *205*, No. 123929.
(51) Li, L.; Ji, P.; Zhang, Y. Molecular Dynamics Simulation of Condensation on Nanostructured Surface in a Confined Space. *Appl. Phys. A: Mater. Sci. Process.* **2016**, *122* (5), 496.
(52) Xu, W.; Lan, Z.; Peng, B. L.; Wen, R. F.; Ma, X. H. Effect of Nano Structures on the Nucleus Wetting Modes during Water Vapour Condensation: From Individual Groove to Nano-Array Surface. *RSC Adv.* **2016**, *6* (10), 7923−7932.

(53) Wang, S.-Y.; Wang, Z.-J.; Wang, D.-Q.; Yang, Y.-R.; Zheng, S.-F.; Gao, S.-R.; Wang, X.-D.; Lee, D.-J. Nucleation of Water Vapor on Nanodimpled Surfaces: Effects of Curvature Radius and Surface Wettability. *Appl. Therm. Eng.* **2023**, *219*, No. 119437.
(54) Wang, Z.; Qin, F.; Luo, X. Numerical Investigation of Effects of Curvature and Wettability of Particles on Heterogeneous Condensation. *J. Chem. Phys.* **2018**, *149* (13), 134306.
(55) Niu, D.; Tang, G. Molecular Dynamics Simulation of Droplet Nucleation and Growth on a Rough Surface: Revealing the Microscopic Mechanism of the Flooding Mode. *RSC Adv.* **2018**, *8* (43), 24517−24524.
(56) Gao, S.; Liao, Q.; Liu, W.; Liu, Z. Effects of Solid Fraction on Droplet Wetting and Vapor Condensation: A Molecular Dynamic Simulation Study. *Langmuir* **2017**, *33* (43), 12379−12388.
(57) Suh, D.; Yasuoka, K. Nanoparticle Growth Analysis by Molecular Dynamics: Spherical Seed. *J. Phys. Chem. B* **2011**, *115* (36), 10631−10645.
(58) Suh, D.; Yasuoka, K. Nanoparticle Growth Analysis by Molecular Dynamics: Cubic Seed. *J. Phys. Chem. B* **2012**, *116* (50), 14637−14649.
(59) Suh, D.; Yasuoka, K.; Zeng, X. C. Molecular Dynamics Simulation of Heterogeneous Nucleation on Nanotubes. *RSC Adv.* **2015**, *5* (51), 40953−40963.
(60) Suh, D.; Yasuoka, K. Condensation on Nanorods by Molecular Dynamics. *J. Chem. Phys.* **2016**, *144* (24), 244702.
(61) Jung, J.; Jang, E.; Shoaib, M. A.; Jo, K.; Kim, J. S. Droplet Formation and Growth inside a Polymer Network: A Molecular Dynamics Simulation Study. *J. Chem. Phys.* **2016**, *144* (13), 134502.
(62) Castillo, J. E.; Weibel, J. A.; Garimella, S. V. The Effect of Relative Humidity on Dropwise Condensation Dynamics. *Int. J. Heat Mass Transfer* **2015**, *80*, 759−766.
(63) Cassie, A. B. D.; Baxter, S. Wettability of Porous Surfaces. *Trans. Faraday Soc.* **1944**, *40* (0), 546−551.
(64) Varanasi, K. K.; Hsu, M.; Bhate, N.; Yang, W.; Deng, T. *Spatial Control in the Heterogeneous Nucleation of Water*. MIT Web Domain, 2009.
(65) Mandsberg, N. K. Spatial Control of Condensation: The Past, the Present, and the Future. *Adv. Mater. Interfaces* **2021**, *8* (23), 2100815.
(66) Plimpton, S. Fast Parallel Algorithms for Short-Range Molecular Dynamics. *J. Comput. Phys.* **1995**, *117* (1), 1−19.
(67) Foiles, S. M.; Baskes, M. I.; Daw, M. S. Embedded-Atom-Method Functions for the Fcc Metals Cu, Ag, Au, Ni, Pd, Pt, and Their Alloys. *Phys. Rev. B* **1986**, *33* (12), 7983−7991.
(68) Berendsen, H. J. C.; Grigera, J. R.; Straatsma, T. P. The Missing Term in Effective Pair Potentials. *J. Phys. Chem.* **1987**, *91* (24), 6269−6271.
(69) Varilly, P.; Chandler, D. Water Evaporation: A Transition Path Sampling Study. *J. Phys. Chem. B* **2013**, *117* (5), 1419−1428.
(70) Ryckaert, J.-P.; Ciccotti, G.; Berendsen, H. J. C. Numerical Integration of the Cartesian Equations of Motion of a System with Constraints: Molecular Dynamics of n-Alkanes. *J. Comput. Phys.* **1977**, *23* (3), 327−341.
(71) Alberts, B.; Johnson, A.; Lewis, J.; Raff, M.; Roberts, K.; Walter, P. *The Lipid Bilayer*. In Molecular Biology of the Cell, 4th ed.; Garland Science, 2002.
(72) Jeong, D.-W.; Jang, H.; Choi, S. Q.; Choi, M. C. Enhanced Stability of Freestanding Lipid Bilayer and Its Stability Criteria. *Sci. Rep.* **2016**, *6* (1), 38158.
(73) Zhu, C.; Gao, Y.; Li, H.; Meng, S.; Li, L.; Francisco, J. S.; Zeng, X. C. Characterizing Hydrophobicity of Amino Acid Side Chains in a Protein Environment via Measuring Contact Angle of a Water Nanodroplet on Planar Peptide Network. *Proc. Natl. Acad. Sci. U. S. A.* **2016**, *113* (46), 12946−12951.
(74) Heldt, C. L.; Zahid, A.; Vijayaragavan, K. S.; Mi, X. Experimental and Computational Surface Hydrophobicity Analysis of a Non-Enveloped Virus and Proteins. *Colloids Surf. B Biointerfaces* **2017**, *153*, 77−84.
(75) Allen, M. P.; Tildesley, D. J. *Computer Simulation of Liquids*; Clarendon Press, 1989.
(76) Stukowski, A. Visualization and Analysis of Atomistic Simulation Data with OVITO−the Open Visualization Tool. *Model. Simul. Mater. Sci. Eng.* **2010**, *18* (1), No. 015012.
(77) Stillinger, F. H., Jr. Rigorous Basis of the Frenkel-Band Theory of Association Equilibrium. *J. Chem. Phys.* **1963**, *38* (7), 1486−1494.
(78) Wang, J.; Chen, S.; Chen, D. Spontaneous Transition of a Water Droplet from the Wenzel State to the Cassie State: A Molecular Dynamics Simulation Study. *Phys. Chem. Chem. Phys.* **2015**, *17* (45), 30533−30539.
(79) Shen, J.-F.; Wu, C.-M.; Li, Y.-R. Microscopic Insight into Mechanisms of Heat and Mass Transfer Improvement of Dropwise Condensation on a Modified Nanopillar Surface. *Int. J. Heat Mass Transfer* **2024**, *219*, No. 124872.

https://doi.org/10.1021/acsami.5c01789
ACS Appl. Mater. Interfaces 2025, 17, 27829−27838